Editors' Suggestion

Spatiotemporal Dynamics of Coral Polyps on a Fluidic Platform

Shuaifeng Li,[1] Liza M. Roger,[2] Judith Klein-Seetharaman,[3] Nastassja A. Lewinski,[2] and Jinkyu Yang[1,*]

[1] *Department of Aeronautics and Astronautics, University of Washington, Seattle, Washington, USA*
[2] *Chemical and Life Science Engineering, Virginia Commonwealth University, Richmond, Virginia, USA*
[3] *School of Molecular Sciences, Arizona State University, Phoenix, Arizona, USA*

(Received 26 February 2022; revised 27 June 2022; accepted 13 July 2022; published 30 August 2022)

Reef-building corals are inherently sessile organisms. However, motion is an important behavioral trait of coral polyps, which plays an essential role in feeding, competition, defense, reproduction, and thus, survival and fitness. Notwithstanding the importance of inherent temporal and spatial multiscale features of polyps, their quantitative properties and modeling still remain challenging and unexplored. Here, we observe *Pocillopora acuta in vivo* under different light and temperature conditions using a fluidic platform that allows the direct microscopic study of small live coral fragments, where the stochastic dynamics of the in-plane waving motion of polyps is uncovered. The relationship between polyps on nubbins is described by motion-correlation analysis. Additionally, the fractional Brownian motions of polyps under certain light conditions and temperatures are revealed by the Hurst index via power spectral analysis. Finally, the motion of polyps is modeled by Langevin dynamics, numerically obtained by data-driven parameterization. This combination of experimental observations, numerical analysis, and theoretical modeling opens an avenue to boost our understanding of the biological and physical behaviors of corals in relation to changing environmental conditions.

DOI: 10.1103/PhysRevApplied.18.024078

I. INTRODUCTION

Animal movement is one of the key features in understanding animal behaviors. The rich dynamics of movements in biosystems have been attracting the interest of many researchers in the field of biophysics for their inherent temporal and spatial multiscale features. However, quantifying and characterizing the different types of motion in biological systems remains challenging due to randomness and the intrinsically complex nature [1]. Recently, with the development of tracking techniques and mathematical modeling strategies, the behaviors, foraging strategies, and distributions of animals are well studied. A variety of methodologies to model animal motions are proposed, including, but not limited to, uncorrelated or correlated random walks [1–4], Levy flight [5–9], stochastic differential equation, such as the noted Ornstein-Uhlenbeck process [1,10–14], and hidden Markov models [15,16].

Many biophysical processes can be modeled as Brownian motion. Nevertheless, other processes reveal the existence of anomalous Brownian motion, which is also called fractional Brownian motion [17]. Such Brownian and derivative motions are widely observed not only in biological systems but also in physical systems, such as the dynamics of ultracold atoms [18]; quantum dots [19–21]; nanoelectrodes [22]; heartbeat intervals [23]; and in our daily lives, including fluctuations of climate [24] and economic markets [25]. In biological systems, particularly in subcellular and cellular structures, the motion of proteins or submicron tracers in living cells [26–29], telomere diffusion in the cell nucleus [30], and diffusion in lipid membranes [31–34] are characterized by fractional Brownian motions. However, the efficacy of such fractional Brownian motion to model the behavior of clonal and colonial organisms, such as reef-building corals, has not been reported and remains elusive.

Coral reefs, as keystone organisms, support rich and diverse ecosystems, and hold immense ecological and economic value. Coral organisms live in symbiosis with photosynthetic algae and complex assemblages of bacterial, archaeal, and fungal communities [35]. The impacts of anthropogenic activities influence the behavior, physiology, and ecology of corals through the global rise in sea-surface temperatures and ocean acidification [36]. Coral colonies are fixed to the substrate, but polyps display dynamic properties, including temporal motion, and their substructures may play an important role in overall coral health, especially in relation to changing environmental conditions [37]. For example, some soft corals, such as the family of Xeniidae, exhibit a unique rhythmic pulsation,

*jkyang@aa.washington.edu

which functions to enhance photosynthesis by modulating water flow [38,39], while, in many species of scleractinian corals, the motions of polyps and tissue are more subtle or even imperceptible [37]. Erratic behavior may occur on coral polyps and colonies due to abnormal environmental variables. Thus, understanding coral motions will help us to better assess coral health in a proactive manner and understand coral physiology in a changing environment, in terms of light conditions, temperature, pH, and other environmental variables [40–46]. To date, however, the motions of coral polyps remain largely unexplored, and their characterization using appropriate models is in its infancy. To evaluate the effect of environmental variables on coral motion, the fluidic platform is necessary for the study of coral motion *in vivo* at the microscale [47,48].

To this end, we design a fluidic platform that allows us to observe the coral nubbin *in vivo* in real time under the microscope, so that the subtle in-plane waving motion of polyps can be captured for analysis. We conduct multiple observations of coral nubbins under different light conditions and temperatures to demonstrate how polyps adjust their motions in response to these conditions. We find that both light (wavelength) and temperature impact polyp motions and modulate behaviors based on differences in correlation, phase synchronization, and the Hurst index of stochastic motion processes. Moreover, we utilize the generalized Langevin equation to model the polyps' motion under different light conditions and temperatures. This unique combination of studying coral behaviors and describing it with mathematical models can boost our understanding of coral physiology and promote the simulation and prediction of coral behavior in response to a given environmental condition in the future.

II. EXPERIMENTAL SYSTEM

Figure 1(a) shows the schematic of our octagonal fluidic platform with a coral nubbin in the chamber. Our fluidic platform, manufactured through three-dimensional (3D) printing, is shown in the inset with the tubing connectors attached. The full design is explained in Appendix A. It is centered around a main chamber surrounded by eight valves and in- and outflow channels that can be opened or closed individually. The valves can control the flow of fluid. Therein, in Fig. 1(a), since the valves shaded in yellow are open, the flow direction of fluid is along a straight path, as shown in blue. The computational fluid-dynamics simulation of this fluidic platform is shown in Appendix A. The velocity field shows the low impact on the coral

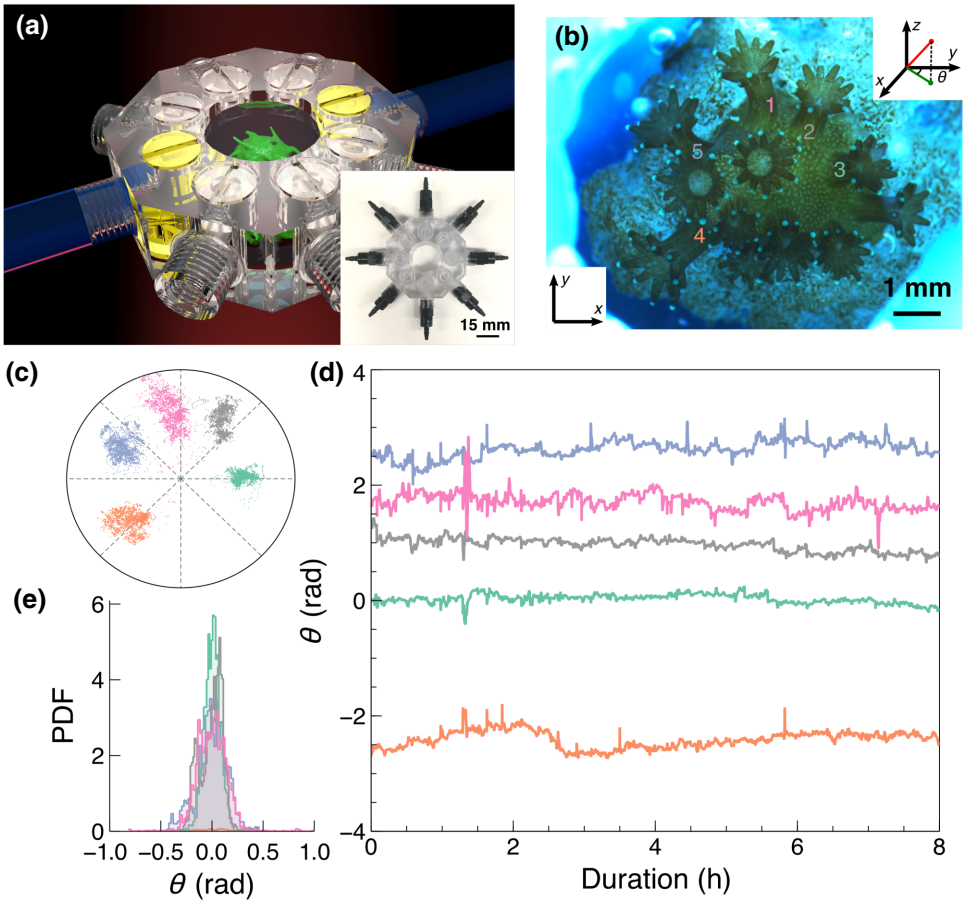

FIG. 1. Experimental observation of coral in the fluidic platform. (a) Schematic of our octagonal fluidic platform with a coral nubbin in the chamber. Inset shows our octagonal fluidic platform for experiment made by 3D printing with VeroClear resin. Valves control the flow of fluid. (b) Coral nubbin observed under the microscope under normal light conditions and 25 °C. Polyps being analyzed in this case are labeled by numbers and color codes used in subsequent figures. (c) Trajectory of polyps. (d) Azimuthal angles, θ, of different polyps as a function of duration. (e) Probability density function of the azimuthal angles, θ, of different polyps after being centered on zero. Colors in (c)–(e) correspond to the colors of labels in (b).

nubbin induced by the water flow to ensure that the spontaneous motion of polyps can be observed. The experimental setup and procedure are shown in Appendix A.

Figure 1(b) shows the coral nubbin under the microscope, where the coral nubbin with several polyps can be observed. This picture is taken of the experimental setup under normal light and 25 °C. A time-lapse video with 300-times playback, illustrating the polyps' motions, is shown in Video 1. The polyps are moving vibrantly, with motions including contraction, extension, and waving. Since we observe the motion right above the coral nubbin, only the orthogonal projection of three-dimensional polyps' motion is recorded. Each polyp is simplified for analysis as a line segment connecting the tentacle crown to the foot of the polyp, so that the azimuthal angle can be calculated with respect to the horizontal direction. The tentacle crown and foot of the polyp are tracked using the correlation-based algorithm [49]. The azimuthal angle, θ, shown in the inset of Fig. 1(b) is found to be appropriate in describing the original motion. Therefore, the azimuthal angle representing the in-plane waving motion of the polyp is used for analysis and discussion here. Note that the other two components, polar angle and radius distance, which represent out-of-plane waving motion and contraction-extension motion, respectively, are lacking detailed information to be determined.

Figure 1(c) exhibits the trajectories of the tentacle crowns of the polyps in different colors, corresponding to the labels in Fig. 1(b). Each of them covers a certain area within the random pattern. Since we study only the in-plane waving motions of polyps, we extract information on the azimuthal angle and show it in Fig. 1(d). These motion signals are all oscillating over time with several spikes at some time periods. Additionally, these signals do not exhibit certain trends, indicating the polyps are randomly moving around their central points. Therefore, as expected, the probability density functions (PDFs) of these motion signals after being centered on zero exhibit symmetric shapes, as shown in Fig. 1(e). The PDFs indicate that most motions are around the central points.

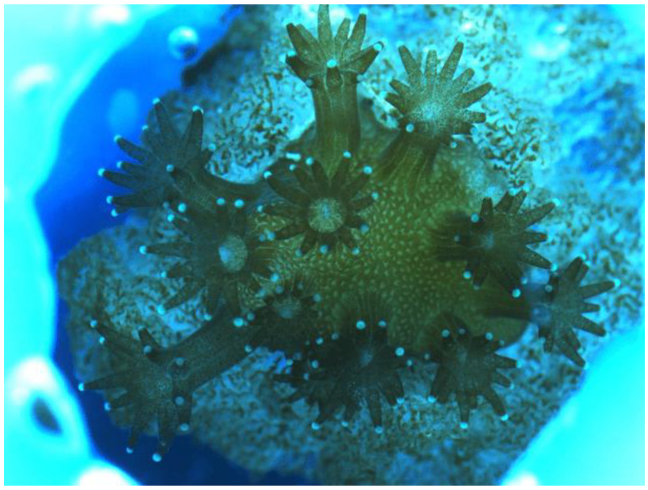

VIDEO 1. Time-lapse video of the coral nubbin under normal light and 25 °C.

III. NUMERICAL ANALYSIS

A. Motion correlation of polyps

Since there are several polyps on one coral nubbin, it is interesting and natural to study the coordination of polyps' motions, if the whole coral nubbin is considered as a colony of interconnected polyps. The motion correlation between polyp m and polyp n can be calculated as

$$r_{mn} = \frac{\sum(\theta_i^m - \overline{\theta^m})(\theta_i^n - \overline{\theta^n})}{\sqrt{\sum(\theta_i^m - \overline{\theta^m})^2 \sum(\theta_i^n - \overline{\theta^n})^2}}, \tag{1}$$

where i and the upper bar denote the index number and the average of the temporal data. As displayed in Fig. 2(a), the positive correlation coefficient indicates the correlated relationship between two polyps, while the negative one suggests the anticorrelated relationship. The correlated or anticorrelated relationship indicates the synchrony of two polyps in terms of movement direction. Additionally, the correlation coefficient changes as a function of light conditions. Compared with the polyps' motions under normal light, which is the control group, the absolute values of the correlation coefficient increase with increasing wavelength. This implies that the in-plane waving-motion trends of polyps on one coral nubbin (i.e., in very close proximity) become more and more pronounced (whether correlated or anticorrelated) when the light shifts from blue light to red light. When the polyps are under normal light, they generally show a stronger trend (correlation or anticorrelation) compared to single-wavelength conditions. Specifically, the case under blue light is significantly different from the other cases in correlated motion ($p = 0.0043$).

We also study the effect of temperature on the correlation between polyps on the same coral nubbin, as shown in Fig. 2(b). The experimental groups (15 and 30 °C) have slight changes in comparison with the control group (25 °C), where the absolute values of the correlation coefficient become smaller with increasing temperature. But for both correlation and anticorrelation, no significant difference is found according to the p value. This indicates stronger trends, more and more correlated or anticorrelated, of in-plane waving motions of polyps at lower temperature.

Apart from correlation, phase synchronization is another important feature to describe the synchrony between two motion signals. The phase denotes the angle corresponding to the momentary deflection of an oscillation. Phase

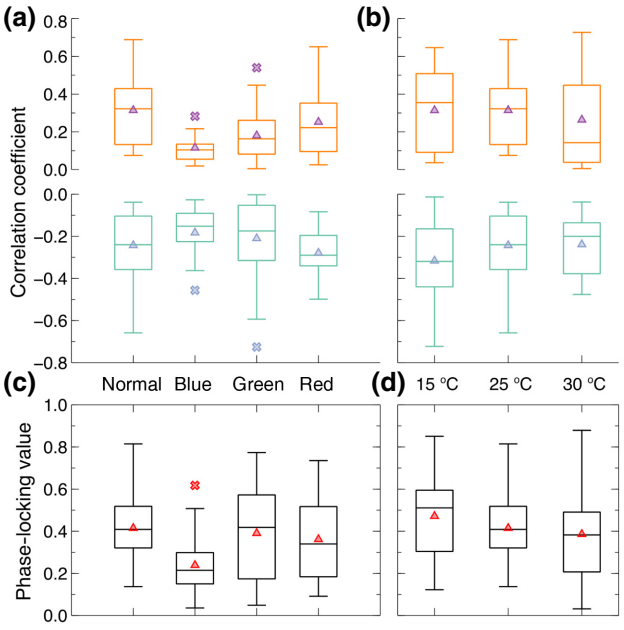

FIG. 2. Analysis of correlation and phase synchronization. (a) Correlation coefficients between polyps on the same coral nubbin under different light conditions (wavelength). Correlations and anticorrelations are shown in orange and green, respectively. (b) Correlation coefficients between polyps on the same coral nubbin under different temperatures. Correlations and anticorrelations are shown in orange and green, respectively. (c) Phase-locking value characterizing phase synchronization between polyps on the same coral nubbin under different light conditions. (d) Phase-locking value characterizing phase synchronization between polyps on the same coral nubbin under different temperatures. Cross and triangle symbols in (a)–(d) represent the outliers and mean, respectively.

synchronization, as a nonlinear measure, refers to the correlation of phase values between two in-plane waving motions of polyp m and polyp n, which can be quantified by the phase-locking value (PLV), which is calculated as

$$V_{mn} = \left| \frac{1}{N} \sum_{j=1}^{N} e^{i[\varphi_m(t_j) - \varphi_n(t_j)]} \right|, \tag{2}$$

where φ_m and φ_n are the phases of θ_m and θ_n, which are obtained by Hilbert transform. Figure 2(c) exhibits the PLV as a function of light condition. We notice that, under blue light, the PLV is smaller than the others, suggesting that the phases of in-plane waving motion of polyps are less synchronized than others, similar to the correlation shown in Fig. 2(a). This obvious trend is also verified by the difference in p value between blue light and other light conditions ($p = 0.0001$, 0.0029, and 0.0358 for normal, green, and red light, respectively). Temperature effects on phase synchronization are displayed in Fig. 2(d). As the temperature increases, the PLV decreases, similar to the correlation shown in Fig. 2(b), indicating that at low temperature the polyps' motions have higher phase synchronization. But the temperature effect is not pronounced.

In conclusion, the motions of polyps belonging to the same coral nubbin do not happen in isolation. Instead, they are coordinated in some way. This shows that the connection between polyps provided by the connective tissue (coenosarc) extends to interpolyp motion, which can be analyzed by motion correlation and phase synchronization. As a result, the in-plane waving motions of polyps on the same coral nubbin are rhythmically activated and inhibited, which can be adjusted by light conditions and temperatures.

B. Fractional Brownian motion and its power spectral densities

According to the observation of the polyp trajectories [Figs. 1(c) and 1(e)], the in-plane waving motions of polyps are a Gaussian stochastic process, the covariance function of which is defined as

$$\langle \theta_{t_1} \theta_{t_2} \rangle = D(t_1^{2H} + t_2^{2H} - |t_1 - t_2|^{2H}), \tag{3}$$

where D is the diffusion coefficient, t_1 and t_2 are two points in time, and $H \in (0, 1)$ is the Hurst index. When $H \neq 0.5$, the process is fractional Brownian motion and when $H = 0.5$ the process is standard Brownian motion. This metric provides the possibility to characterize the motion of polyps from the perspective of Brownian motion. First of all, we calculate the power spectral density (PSD) of the single trajectory by

$$S = \frac{1}{T} \left| \int_0^T \theta_t e^{ift} dt \right|^2, \tag{4}$$

where T is the observation time. In total, we obtain multiple ($\geq$15) trajectories for the experiments under each light and temperature condition.

As shown in Fig. 3(a), the PSDs of individual trajectories under different light conditions exhibit straight trends on the logarithmic scale, suggesting the power-law relationship between frequency and PSD. Additionally, the slopes of the PSDs are within certain ranges that can be used to deduce the Hurst index, according to the power-law relationship between frequency and PSD: $S \sim f^{-(2H+1)}$. This type of motion is generally called $1/f$ -type motion. Because the calculated slope for the logarithm-scale graph is smaller than -1, this $1/f$ -type motion is specifically Brownian-type motion. To determine the type of Brownian motion, the Hurst index needs to be calculated. However, since PSD is an ensemble-averaged property, our available experimental data sets are small for such ensemble averages, so the calculated Hurst index may not be accurate. In addition, simply fitting a straight line will give us

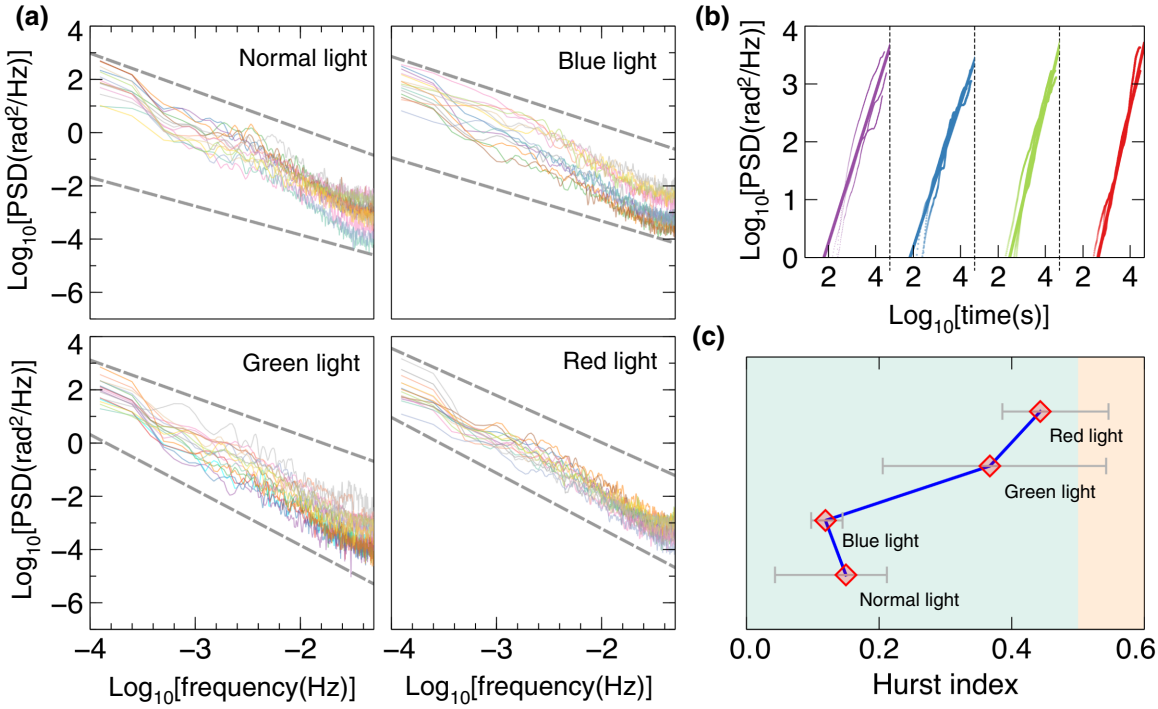

FIG. 3. Power spectrum analysis of experimental data sets under different light conditions. (a) PSD of representative in-plane waving motions represented by the azimuthal angle, θ, under different light conditions. Dashed gray lines show the $1/f^{1.08}$ and $1/f^{1.42}$ trends for normal light, $1/f^{1.19}$ and $1/f^{1.28}$ trends for blue light, $1/f^{1.41}$ and $1/f^{2}$ trends for green light, and $1/f^{1.77}$ and $1/f^{2}$ trends for red light. (b) PSDs evaluated at zero frequency shown in dots for normal light, blue light, green light, and red light from left to right. Solid lines show the fitted results. Both x and y axes are on the logarithmic scale. (c) Hurst indices for cases under normal light, blue light, green light, and red light. Subdiffusion and superdiffusion areas are shaded in green and orange, respectively.

a deceptive result because in standard Brownian motion and fractional Brownian motion when $H > 0.5$, they both have PSDs that scale as f^{-2}. Moreover, the variations in PSDs are so subtle that different fitting methods may lead to different results.

Therefore, the method for calculating the Hurst index from the zero-frequency PSD is applied [30]. The PSD at zero frequency can be expressed as

$$S(f = 0) = \frac{1}{T}\left|\int_0^T \theta_t dt\right|^2, \tag{5}$$

which is simply the squared area under the motion signal, θ_t, divided by T. It is proven that the individual trajectory of the zero-frequency PSD is the gamma distribution with scale 2μ and shape parameter 1/2, where μ is the ensemble-averaged zero-frequency PSD. μ has a power-law relationship with observation time universally (for both subdiffusive and superdiffusive cases) expressed by

$$\mu(f = 0) = \frac{DT^{2H+1}}{H+1}. \tag{6}$$

Therefore, we can easily leverage this relationship to calculate a reliable Hurst index to avoid the drawbacks of directly using PSD mentioned above. As shown in Fig. 3(b), from left to right, the zero-frequency PSDs of θ under normal light, blue light, green light, and red light are increasing as a function of observation time. We notice that on the logarithmic scale they have linear trends (dots) and then are fitted by straight lines (solid lines); this agrees with the dots and coincides with the theory above.

Furthermore, the Hurst index for each case can be extracted, as shown in Fig. 3(c). From this graph, we notice that, in most cases, the Hurst index is less than 0.5 (area shaded in green), indicating the that in-plane waving motions of polyps are subdiffusive in fractional Brownian motion. To entail subdiffusive motion, the increments are negatively correlated, such that it is most likely that after an increasing step a decreasing one will follow. It is obvious in Fig. 3(c) that the in-plane waving motions of polyps under blue light have the smallest Hurst index. With increasing wavelength from blue light to red light, the Hurst index is increasing close to 0.5, which implies that a decreasing step will be less likely to follow an increasing step. Given the power-law relationship between frequency and PSD, the trends of $S \sim f^{-(2H+1)}$ based on the calculated Hurst index from the zero-frequency PSD are illustrated in Fig. 3(a). The gray dashed lines in Fig. 3(a) show the $f^{-1.08}$ and $f^{-1.42}$ trends for normal light, $f^{-1.19}$

and $f^{-1.28}$ trends for blue light, $f^{-1.41}$ and f^{-2} trends for green light, and $f^{-1.77}$ and f^{-2} trends for red light. It turns out that the estimated PSD and the PSDs of individual trajectories of polyps show good agreement.

Similarly, the PSDs under different temperatures are shown in Fig. 4(a). For the logarithm-scale graphs, PSDs have linear trends, which agree with the power-law relationship between frequency and PSD. As shown in Fig. 4(b), from left to right, the zero-frequency PSDs as a function of time for 15, 25, and 30 °C have linear trends (dots) with fitted straight lines (solid lines). Therefore, we can extract the Hurst index from the slopes of the straight lines. Figure 4(c) shows the Hurst index for 15, 25, and 30 °C, where the control group (25 °C) is in the subdiffusion region. We notice that at 15 and 30 °C the Hurst index is extremely variable, spanning from the subdiffusion region to the superdiffusion region; this suggests an uncertain diffusive mode in in-plane waving motion of polyps outside the optimum thermal range. Likewise, the dashed gray lines in Fig. 4(a) show the $f^{-1.20}$ and f^{-2} trends for 15 °C, $f^{-1.08}$ and $f^{-1.42}$ trends for 25 °C, and $f^{-1.25}$ and f^{-2} trends for 30 °C, to indicate agreement between the estimated PSD and the PSDs of the individual trajectory of polyps.

It should be noted that, under normal conditions (normal light and 25 °C), the Hurst index is around 0.2, which can be set as the baseline. The Hurst index will deviate away from this baseline under other conditions, especially under green and red light or higher and lower temperatures. Under some conditions, the diffusion type is extremely variable, switching from subdiffusion to superdiffusion. The accuracy of the calculation for the Hurst index can be improved by increasing the number of replicates and extending the observation time. We note in passing that the findings presented here are only relevant for *Pocillopora acuta* under the given experimental conditions;

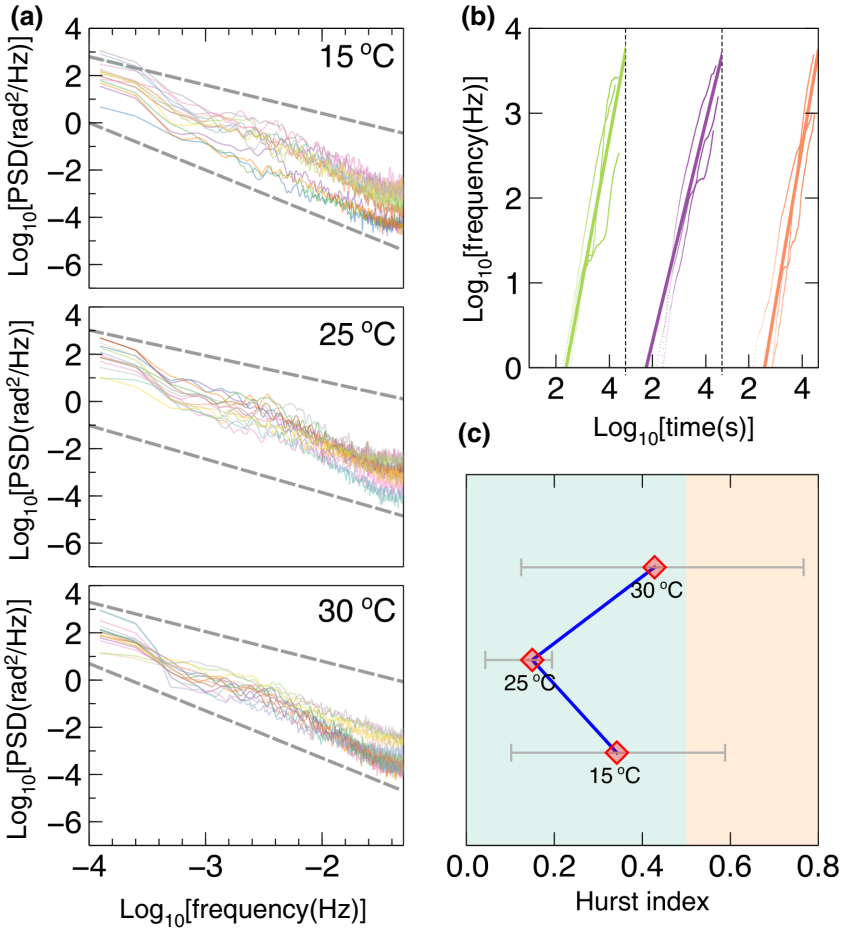

FIG. 4. Power spectrum analysis of experimental data sets under different temperatures. (a) PSD of representative in-plane waving motions represented by the azimuthal angle, θ, under different temperatures. Dashed gray lines show the $1/f^{1.20}$ and $1/f^{2}$ trends for 15 °C, $1/f^{1.08}$ and $1/f^{1.42}$ trends for 25 °C, and $1/f^{1.25}$ and $1/f^{2}$ trends for 30 °C. (b) PSDs evaluated at zero frequency are shown as dots for 15, 25, and 30 °C from left to right. Solid lines show the fitted results. Both x and y axes are on the logarithmic scale. (c) Hurst indices for cases at 15, 25, and 30 °C. Subdiffusion and superdiffusion areas are shaded in green and orange, respectively.

the extension to other reef-building corals under various conditions can be explored in the future.

IV. THEORETICAL MODELING VIA LANGEVIN DYNAMICS

According to the discussion above, the in-plane waving motions of polyps are fractional Brownian motion that is affected by light conditions and temperatures. This stochastic Brownian process can be modeled using the generalized Langevin equation without a conservative force term, which can be expressed by

$$\ddot{\theta} = -\int_0^t K(t-\tau)\dot{\theta}(\tau)d\tau + R(t), \tag{7}$$

where K is the memory-kernel function, and $R(t)$ is the random-noise term with zero mean, satisfying the second fluctuation-dissipation theorem [50]: $\langle R(t)R(t')\rangle = k_B T K(t-t')$, where k_B denotes the Boltzmann constant. Hence, the main focus is to model the memory-kernel function and the random-noise term. Here, we use the data-driven method to discover the parameterization of the generalized Langevin equation [51,52]. The generalized Langevin equation becomes $G(t) = -\int_0^t K(t-\tau)H(\tau)d\tau$ after $\dot{\theta}(0)^T$ is right-multiplied to the generalized Langevin equation. Note that the correlation matrices are $G(t) = \langle\ddot{\theta}\dot{\theta}(0)^T\rangle$, $H(t) = \langle\dot{\theta}\dot{\theta}(0)^T\rangle$, and $\langle R(t)\dot{\theta}(0)^T\rangle = 0$ [53]. However, this equation may lead to an unreliable solution due to the integral equation of the first kind [51]. We then obtain $\hat{G}(\zeta) = -\hat{K}(\zeta)\hat{H}(\zeta)$ by conducting the Laplace transform, where the hat means the Laplace transform of the corresponding functions. The memory-kernel function at the Markovian limit, $\hat{K}(\infty)$, also known as the friction tensor, is estimated to compare each experimental setup. As shown in Fig. 5(a), $\hat{K}(\infty)$, calculated by

$$\hat{K}(\infty) = -\hat{G}(\infty)\hat{H}(\infty) = -\left(\int_0^\infty G(t)dt\right)\left(\int_0^\infty H(t)dt\right)^{-1}, \tag{8}$$

is summarized for different light conditions. From Fig. 5(a), generally, compared with the case under normal light, other cases under blue light and green light have larger memory-kernel function on average. In experimental groups, the memory-kernel functions of most cases are smaller under the red light than those under the other light conditions. Physically, $\hat{K}(\infty)$ is a dissipation term and should be inversely proportional to motion correlation (Fig. 2) and the Hurst index (Fig. 3). The memory-kernel function can also be estimated from the rational function in different orders. Details on the calculation of the memory-kernel function are shown in Appendix B.

Once we determine the memory-kernel function, the next step is to estimate the random-noise term. The non-Markovian nature of fractional Brownian motion makes computations and simulations difficult. Therefore, we define the auxiliary variable, $d(t) = -\int_0^t \hat{K}(t-\tau)\dot{\theta}(\tau)d\tau + R(t)$. For simplicity, the demonstration of the motion simulation is based on the first-order approximation, where the auxiliary variable can be simplified as $d(t) = -\int_0^t A_1 e^{B_1(t-\tau)}\dot{\theta}(\tau)d\tau + R(t)$, which can be further expressed in terms of coefficients in a first-order approximation of A_1, B_1, and white noise W:

$$\begin{aligned}\ddot{\theta} &= d,\\ \dot{d} &= B_1 d - A_1\dot{\theta} + W.\end{aligned} \tag{9}$$

The probability density function of W is characterized by a peak in small values and rapidly decays to large values (Appendix C). Since direct fitting of distributions on the histogram and a visual comparison with the assumed distribution are shown to be unreliable [54], we use the maximum-likelihood method to determine the optimal parameter for several distribution candidates, (a) $\rho_\lambda(W) = ce^{-\lambda|W|}$, (b) $\rho_\mu(W) = c|W|^{-\mu}$, and (c) $\rho_\sigma(W) = \left(1/\sqrt{2\pi\sigma^2}\right)e^{-(W^2/2\sigma^2)}$, which are the exponential distribution, power-law distribution, and normal distribution, respectively. After determining the optimal parameter by the maximum-likelihood method, the Akaike information criterion and the Bayesian information criterion are used to determine the most appropriate function to model the white-noise term [55]. It turns out that the exponential distribution is the preferred model for the white-noise term (see Appendix C). Figure 5(b) exhibits the parameter λ for the exponential distribution under different light conditions. Compared with normal light, the parameters are larger under green light, which results in clear differences in the exponential distribution using the average parameter λ under different light conditions [Fig. 5(c)]. Likewise, the model of white noise of in-plane waving motion of polyps at different temperatures is shown in Appendix D and clearly demonstrates the distinction for different temperatures.

The next step is to simulate the in-plane waving motion of polyps under different light conditions and temperatures based on the generalized Langevin dynamics. Here, Fig. 5(d) shows the simulated results under normal light and 25 °C spanning around 5.5 h, which are clearly stochastic. The Hurst indices are shown below the curves with typical subdiffusion nature, where the Hurst index is less than 0.5. To check the statistical similarity between our simulated results and experimental results, the PDFs of corresponding in-plane waving motions are exhibited on the right panel of Fig. 5(d). PDFs with characteristic bell-shaped curves can be observed, which are consistent with the PDF trends shown in Fig. 1(e).

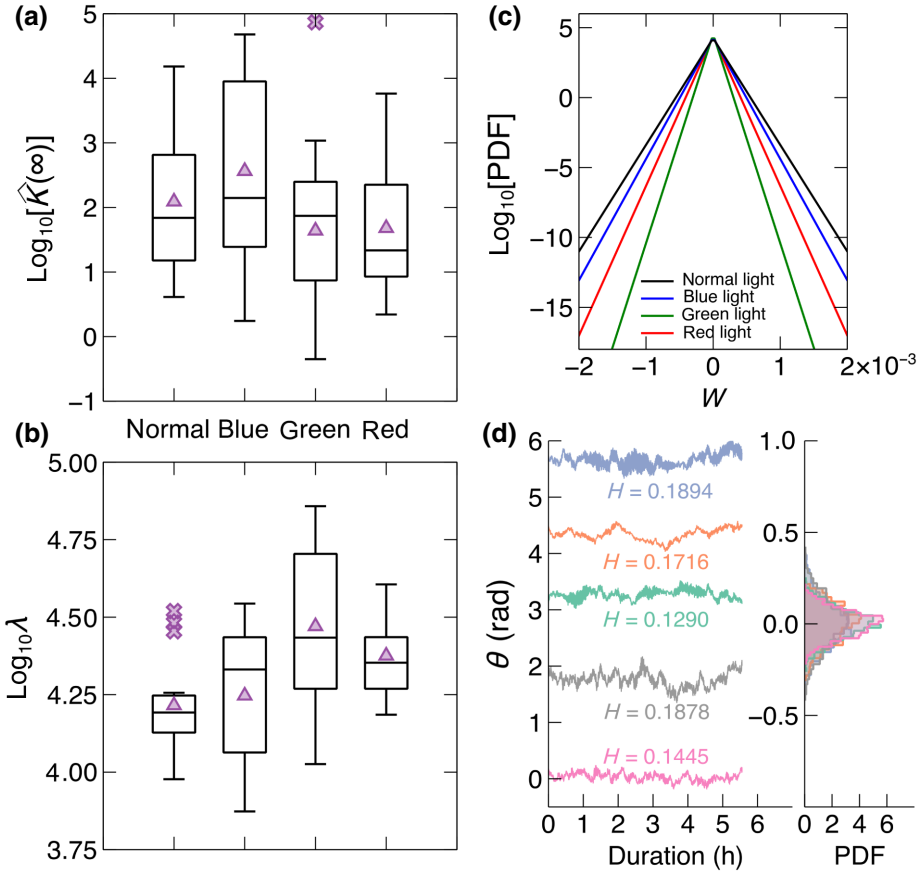

FIG. 5. Model of the in-plane waving motion of coral polyps under different light conditions. (a) Value of the memory-kernel function at the Markovian limit, $\hat{K}(\infty)$, of polyps under normal, blue, green, and red light. (b) Parameter λ for the exponential distribution to model the white-noise term under normal, blue, green, and red light. (c) Fitted PDF of the white-noise terms under different light conditions by using the average parameter λ. (d) Simulated in-plane waving motions of five polyps under normal light and 25 °C based on the generalized Langevin equation. Hurst indices are shown below the simulated results. Corresponding PDFs of simulated results are exhibited on the right panel. Cross and triangle symbols in (a),(b) represent the outliers and mean, respectively.

V. CONCLUSION AND DISCUSSION

Here, we test the hypothesis that the motions of corals are affected by abiotic factors, such as light and temperature, in the context of environmental change. To test this hypothesis, we design a fluidic platform to observe the motions of coral at the scale of single polyps experimentally. This allows us to explore the in-plane waving motion through correlation and synchronization analyses, resulting in the correlated and phase-synchronized motion of polyps on the same coral nubbin, which is affected by light and temperature. In addition, the in-plane waving motions of polyps are found to be fractional Brownian motion with a Hurst index generally smaller than 0.5 from the power spectral density analysis. Outside of optimal growth conditions (normal light and 25 °C), the Hurst index becomes highly variable (spanning between diffusive, subdiffusion, and superdiffusion modes) with a baseline index of about 0.2. Finally, the model of in-plane waving motion of polyps is established for different light conditions and temperatures using the Langevin dynamics, which statistically agrees well with experimental results. The memory-kernel function and noise term are calculated by data-driven methods, in which the light conditions and temperatures also play important roles.

Increasing temperature and decreasing wavelength can both be, respectively, associated with global warming and sea-level rise, since it is well known that longer wavelengths (red light) have only shallow penetration in the ocean compared to shorter wavelengths (blue light). With global sea-level rise, corals face a shift in light composition to more blue light, which will probably weaken or even reverse the current in-plane waving-motion trends of polyps and potentially entire colonies in the future. Based on the present results, future research directions could include the following. The impact from other environmental variables could be explored based on our fluidic platform and methods. Additionally, the specific biological functions of polyp motion remain unclear. Movement of

polyps may facilitate water flow and photosynthesis similarly to tentacle motion. Another possibility is that this Brownian-type motion may benefit the foraging strategy. Apart from coral polyps, coral-tentacle motion could also be theoretically modeled by our methods. Furthermore, machine-learning techniques, which are suitable for big-data analysis and modeling, may be developed to study coral behaviors. It is also possible to apply our method in the field, requiring a shorter observation time and higher frequency of taking images to ensure the collection of high-quality images. Citizen-science and shared-data-repository approaches can be potentially leveraged.

Our research, with scaled experimental observations, numerical analysis, and theoretical modeling, paves the way to study the motion of polyps, clonal, and colonial organisms and boost our understanding of the impacts of abiotic factors on the behavior of coral polyps and coral colonies as a whole. The modeling of spatiotemporal dynamics of coral polyps may have promising applications in constructing more realistic scenes in virtual reality and the prediction of coral behavior in response to environmental change.

The code for data analysis is available in the Open Science Framework [56].

ACKNOWLEDGMENTS

The authors would like to thank Adam P. Hamel of VCU's Innovation Lab and Philippe Roger for their advice during the testing and design phases of the octagonal fluidic platform. This work is supported by funding from the National Science Foundation (HDR, DIRSE-IL, Grants No. 1939249, No. 1940169, and No. 1939699).

APPENDIX A: EXPERIMENTAL METHODS

1. Design and fabrication of the octagonal fluidic platform

The octagonal fluidic platform is designed using the computer-assisted drawing software SOLIDWORKS. The design is 3D printed using a Polyjet 3D printer (Objet Eden 260VS) with VeroClear resin (clear and transparent resin, to allow for light penetration). This fluidic platform is specifically designed for the *in vivo* study of small coral fragments (i.e., nubbins, $\leq$5 mm) as opposed to typical large fragments used (5–10 cm). During printing, the main chamber is open on both faces (top and bottom), which enables its attachment (glue) onto glass slides of various thicknesses for top and/or bottom imaging.

2. Experimental setup and procedure

Coral nubbins ($\leq$5 mm) are cut from larger fragments of *Pocillopora acuta*, glued onto glass coverslips, and placed back into tanks to recover for two months [48]. For the experiments, the nubbins are placed in the octagonal fluidic platform (one at a time) under a dissecting microscope (magnification is varied according to the size of the nubbin) mounted with a Nikon camera and viewing tablet. Photos are taken every 10 s from day 1 until the end of the experiment and assembled as a time series for analysis. The octagonal fluidic platform is connected to a peristaltic pump that transports the seawater (salinity, specific gravity = 1.025) from the holding vessel to the chamber (holding vessel under constant stirring at 300 rpm and heating). A low flow rate ($\sim$5 μl/s) is maintained to avoid impacting on polyp motion while still regularly renewing the artificial seawater inside the chamber. The computational fluid-dynamics simulation with different flow rates are exhibited in Fig. 6, where lower impact is observed at a flow rate of 5 μl/s.

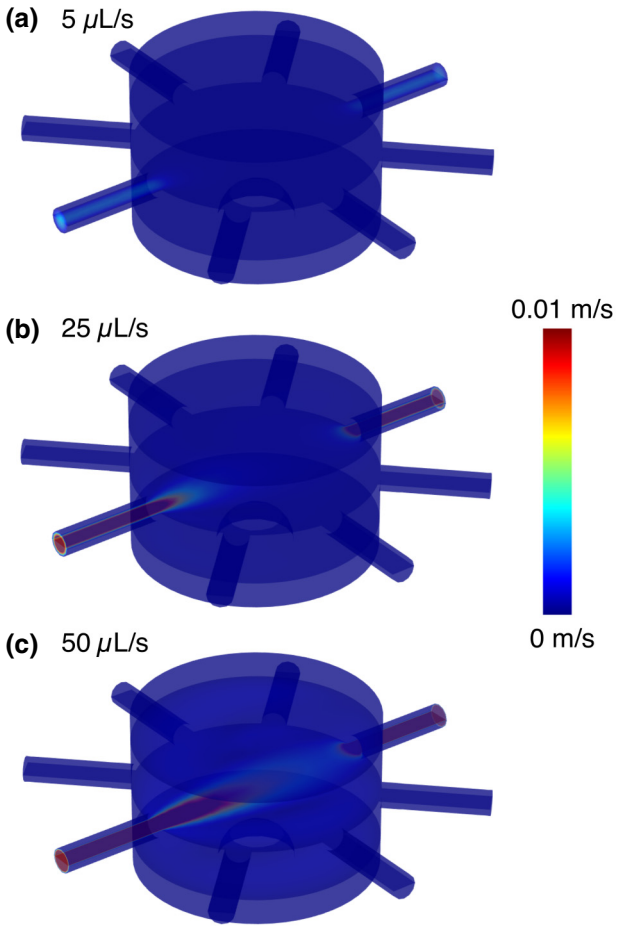

FIG. 6. Computational fluid-dynamics simulation with different flow rates of our fluidic platform. Velocity distribution of the fluid is shown in the tubes and chamber. Three slices are shown in the chamber, one of which shows the velocity distribution near the coral nubbin. Results of using flow rates of 5, 25, and 50 μl/s are shown in (a)–(c), respectively.

The AI Prime™ 16HD reef light system is used as the light source with constant power but adjustable wavelengths on a 10/14 h daylight cycle. To make sure the corals acclimate to the fluidic environment, we move the nubbins from the aquarium to the chamber on day 1 under normal light and temperature. On day 2, light and temperature are adjusted to the experimental conditions and maintained for 24 h. On day 3, the conditions are returned to normal, and the nubbin is placed back into the aquarium at the end of the day. The experimental settings include normal, blue, green, and red light at temperatures of 25, 15, 25, and 30 °C. Blue, green, and red light are monochromatic but normal light is mixed with 7% UV, 7% violet, 7% royal blue, 7% blue, 7% green, 19% deep red, 7% moonlight, and 33% cool white, according to the light settings on the AI Prime™ 16HD reef light system. Note that each experimental setting is replicated three times.

APPENDIX B: DATA-DRIVEN PARAMETERIZATION OF THE LANGEVIN EQUATION

One of the main focuses of the generalized Langevin equation is to estimate the memory-kernel function. We use the data-driven method to estimate the memory-kernel function. As mentioned in the main text, after we obtain $G(t) = -\int_0^t K(t-\tau)H(\tau)d\tau$, we conduct the Laplace transform to obtain $\hat{G}(\zeta) = -\hat{K}(\zeta)\hat{H}(\zeta)$. Note that we work with the variable ζ instead of the usual choice of $s(s = 1/\zeta)$, so that we obtain $\mathcal{L}(G(t)) = \hat{G}(\zeta) = \int_0^\infty G(t)e^{-t/\zeta}dt$, $\mathcal{L}(H(t)) = \hat{H}(\zeta) = \int_0^\infty H(t)e^{-t/\zeta}dt$, and $\mathcal{L}(K(t)) = \hat{K}(\zeta) = \int_0^\infty K(t)e^{-t/\zeta}dt$. By integrating by parts repeatedly, we can obtain the relationship between the variable before and after the Laplace transform:

$$\begin{aligned} \hat{G}^{(i)}(0) &= i!G^{(i-1)}(0), \\ \hat{H}^{(i)}(0) &= i!H^{(i-1)}(0), \\ \hat{K}^{(i)}(0) &= i!K^{(i-1)}(0). \end{aligned} \tag{B1}$$

Additionally, when taking $\zeta \to \infty$, we can obtain the Markovian limit of these parameters: $\lim_{\zeta\to\infty} \hat{G}(\zeta) = \int_0^\infty G(t)dt$, $\lim_{\zeta\to\infty} \hat{H}(\zeta) = \int_0^\infty H(t)dt$, and $\lim_{\zeta\to\infty} \hat{K}(\zeta) = \int_0^\infty K(t)dt$. Therefore, the memory-kernel function at the Markovian limit, $\hat{K}(\infty)$, can be calculated by

$$\hat{K}(\infty) = -\hat{G}(\infty)\hat{H}(\infty) = -\left(\int_0^\infty G(t)dt\right) \times \left(\int_0^\infty H(t)dt\right)^{-1}. \tag{B2}$$

To calculate $\hat{K}(\zeta)$ for any ζ, we use a rational function approximation for $\hat{K}(\zeta)$ in the form of

$$\hat{K}(\zeta) = \left(I - \sum_{m=1}^{M} B_m \zeta^m\right)^{-1} \left(\sum_{m=1}^{M} A_m \zeta^m\right), \tag{B3}$$

where the terms of expression are matrices A_m and $B_m \in \mathbb{R}^{N\times N}$. The highest-order coefficients can be found by taking the limit: $\lim_{\zeta\to\infty} \hat{\mathrm{K}}(\zeta) = -B_M^{-1}A_M$.

$\hat{K}(\zeta)$ can also be expanded by the Taylor expansion at $\zeta = 0$:

$$\hat{K}(\zeta) = \sum_{n=1}^{\infty} \frac{\hat{K}^{(n)}(0)}{n!}\zeta^n. \tag{B4}$$

The rational function approximation for $\hat{K}(\zeta)$ can be matched with the form of the Taylor expansion, which results in

$$\frac{\hat{K}^{(n)}(0)}{n!} = A_n + \sum_{l+m=n} B_l \frac{\hat{K}^{(m)}(0)}{m!}. \tag{B5}$$

Combined with the conversion between variables before and after the Laplace transform, we can deduce the coefficients in the rational function approximation. For

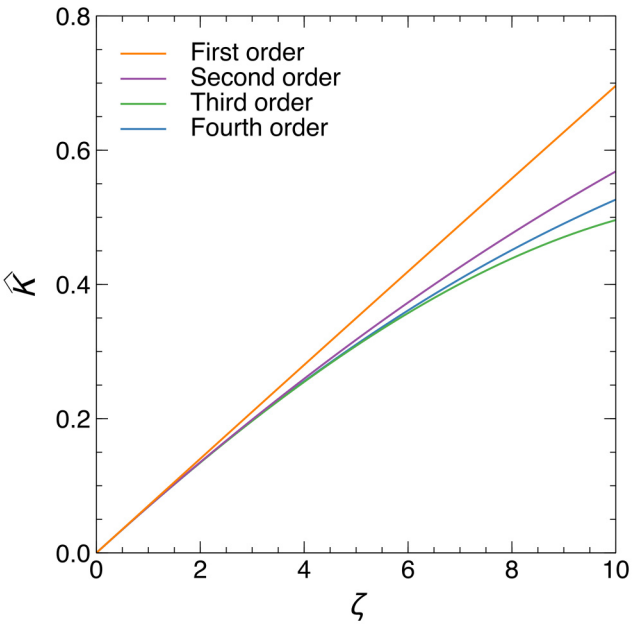

FIG. 7. Laplace transform of the memory kernel for modeling the in-plane motion of coral polyps. First-order, second-order, third-order, and fourth-order estimations of the Laplace transform of the memory kernel are shown in different colors. Third-order and fourth-order estimations overlap. These curves converge to a certain value with the increase of ζ.

example, as for the first-order approximation, $A_1 = -G^{(1)}(0)[H^{(1)}(0)]^{-1}$ and $B_1 = -A_1[\hat{K}(\infty)]^{-1}$. Likewise, we can obtain the coefficients of the higher-order rational function approximation. Then the inverse Laplace transform can be used to obtain the memory-kernel function in the time domain.

We take polyp 3 labeled in Fig. 1(c) as an example. As shown in Fig. 7, the first-order, second-order, third-order, and fourth-order rational function approximations of the memory-kernel function are presented in different colors. We notice that rational function approximations of the memory-kernel function are becoming closer and closer with increasing approximation order, suggesting that the rational function is sufficient to describe the real memory-kernel function.

APPENDIX C: MODELING OF THE STOCHASTIC TERM IN LANGEVIN DYNAMICS BY THE MAXIMUM-LIKELIHOOD METHOD

Since the form of the generalized Langevin equation poses a challenge for further investigation, and $R(t)$ represents the colored-noise term in the generalized Langevin equation, we need to represent the generalized Langevin equation with extended dynamics driven by the white-noise term. For simplicity and demonstration, the first-order approximation of the memory-kernel function is used. Therefore, after the inverse Laplace transform and substitution, we can define the auxiliary variable, $d(t) = -\int_0^t A_1 e^{B_1(t-\tau)}\dot{\theta}(\tau)d\tau + R(t)$. Under the Leibniz rule, $d(t)$ can be differentiated as $\dot{d}(t) = -A_1\dot{\theta}(t) - B_1\int_0^t A_1 e^{B_1(t-\tau)}\dot{\theta}(\tau)d\tau + \dot{R}(t)$. Since $R(t)$ satisfies the second fluctuation-dissipation theorem, $R(t)$ can be expressed as the initial condition, $d(0)$, and the white noise, $W(t)$: $R(t) = \int_0^t e^{B_1(t-\tau)}W(\tau)d\tau + e^{B_1 t}d(0)$. Next, after substitution, $\dot{d}(t)$ can be rewritten as $\dot{d} = B_1 d - A_1\dot{\theta} + W$. Therefore, the in-plane waving motion of the coral polyp under the first-order approximation is governed by Eq. (9). In this way, the in-plane waving motion can be easily simulated by solving this equation set.

As an example, the probability density function of the white-noise term of coral polyp 3 labeled in Fig. 1(b) is shown in Fig. 8. It is difficult to determine the distribution function because this probability density function is similar to some assumed distribution by visual comparison.

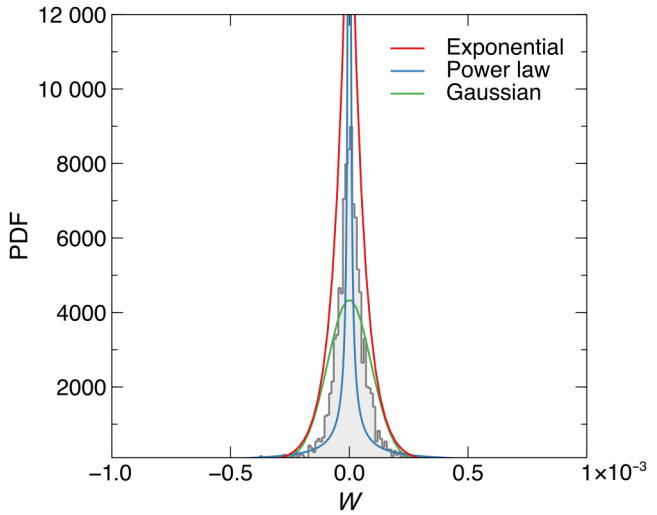

FIG. 8. Probability density function of the white-noise term. Probability density function of the white-noise term, W, is shaded in gray. Red, blue, and green dashed lines show the fitted exponential function, power-law function, and Gaussian function, respectively.

Therefore, the maximum-likelihood method is adopted to determine the optimal parameter, for several distribution candidates, (a) $\rho_\lambda(W) = ce^{-\lambda|W|}$, (b) $\rho_\mu(W) = c|W|^{-\mu}$, and (c) $\rho_\sigma(W) = \left(1/\sqrt{2\pi\sigma^2}\right)e^{-(W^2/2\sigma^2)}$, which are the exponential distribution, power-law distribution, and normal distribution, respectively. Given a set of white-noise terms, $W = \{w_1, w_2, \ldots, w_n\}$, and a probability density function, $\rho_\lambda(W)$, where λ is a vector of k parameters, the log likelihood of the probability density function can be expressed by

$$\ln\ L(\lambda|R) = \ln\prod_{j=1}^{n}\rho_\lambda(r_j) = \sum_{j=1}^{n}\ln\ \rho_\lambda(r_j). \qquad \text{(C1)}$$

For each candidate, we find λ to maximize the log likelihood and obtain the optimal parameters. Herein, the Nelder-Mead simplex search algorithm is used to find the extrema. Three candidates with optimal parameters are exhibited in Fig. 8. We notice that an obviously normal distribution does not fit our probability density function, but the other three distributions are difficult to distinguish.

TABLE I. White-noise model selection for different light conditions. Preferred model for each polyp in each replicated experiment is displayed based on the Akaike information criterion and the Bayesian information criterion.

	Normal light	Blue light	Green light	Red light
Replicate 1	5/5 exponential	4/4 exponential	6/6 exponential	4/4 exponential
Replicate 2	5/5 exponential	5/6 exponential1/6 power law	5/5 exponential	4/4 exponential
Replicate 3	5/5 exponential	5/5 exponential	6/6 exponential	7/7 exponential

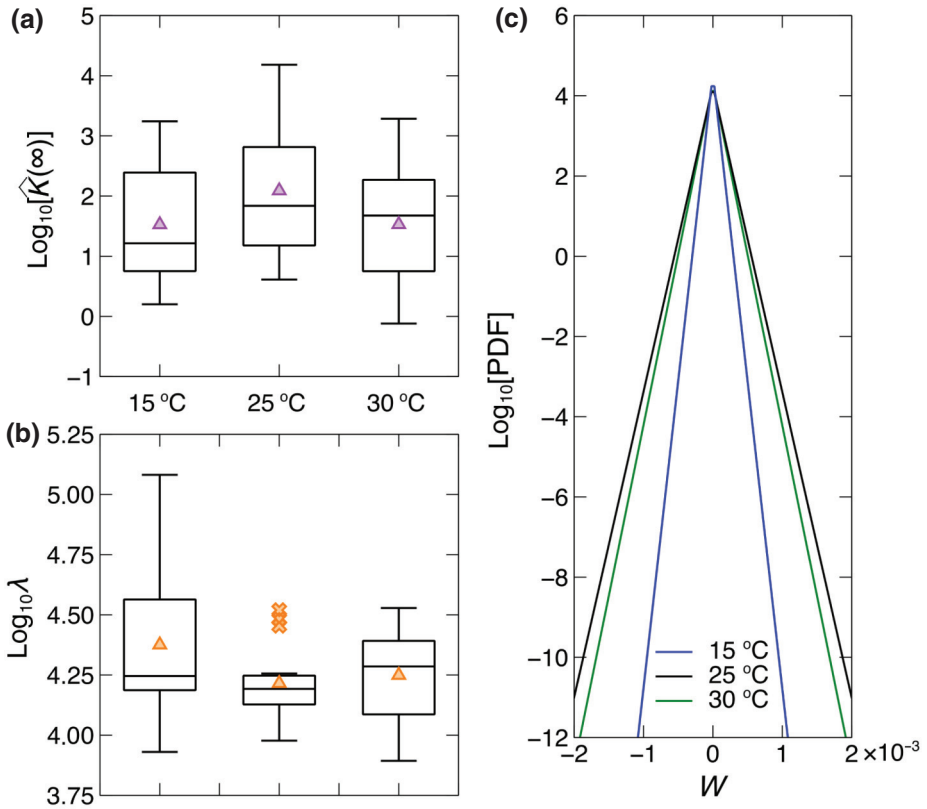

FIG. 9. Model of in-plane waving motion of coral polyps under different temperatures. (a) Value of the memory-kernel function at the Markovian limit, $\hat{K}(\infty)$, of coral polyps at 15, 25, and 30 °C. (b) Parameter λ for the exponential distribution to model the white-noise term at 15, 25, and 30 °C. (c) Fitted PDF of the white-noise terms at different temperatures by using the average parameter λ. Cross and triangle symbols in (a),(b) represent the outliers and mean, respectively.

To find the preference between the different model distributions, the likelihoods, L, of which are maximized, the Akaike information criterion and the Bayesian information criterion, defined as $C_{\mathrm{Ai}} = -2\ \ln\ L + 2k$ and $C_{\mathrm{Bi}} = -2\ \ln\ L + \ln(n)k$, respectively, are used. The most appropriate model can minimize the information criterion. The results show that the Akaike and Bayesian information criteria make no difference for selection of the model (i.e., the Bayesian information criterion agrees with the Akaike information criterion on 100% of all data sets). Table I shows the white-noise model for each polyp under different light conditions. These results show that most of the polyps prefer the exponential distribution to model the white-noise term in the generalized Langevin equation under different light conditions.

APPENDIX D: THE MODEL OF IN-PLANE WAVING MOTION OF CORAL POLYPS AT DIFFERENT TEMPERATURES

We also study the model of in-plane waving motion of coral polyps under different temperatures. Likewise, we obtain the memory-kernel function by the data-driven parameterization and the noise term by the maximum-likelihood method. From Fig. 9(a), generally, compared with the case at normal temperature, other cases at 15 and 30 °C have smaller memory-kernel functions, on average. Figure 9(b) exhibits the parameter λ for the exponential distribution under different light conditions. Compared with normal light, λ is larger at 15 and 30 °C, which results in clear differences in the exponential distribution

TABLE II. White-noise model selection for different temperatures. Preferred model for each polyp in each replicated experiment is displayed based on the Akaike information criterion and the Bayesian information criterion.

	15 °C	25 °C	30 °C
Replicate 1	6/6 exponential	5/5 exponential	5/5 exponential
Replicate 2	5/5 exponential	5/5 exponential	4/5 exponential1/5 power law
Replicate 3	4/4 exponential	5/5 exponential	5/5 exponential

using the average parameter λ at 25 °C [Fig. 9(c)]. Table II shows the white-noise model for each polyp under different temperature conditions. These results show that most of the polyps prefer the exponential distribution to model the white-noise term in the generalized Langevin equation under different temperature conditions.

[1] E. A. Codling, M. J. Plank, and S. Benhamou, Random walk models in biology, J. R. Soc., Interface **5**, 813 (2008).

[2] B. T. McClintock, R. King, L. Thomas, J. Matthiopoulos, B. J. McConnell, and J. M. Morales, A general discrete-time modeling framework for animal movement using multistate random walks, Ecol. Monogr. **82**, 335 (2012).

[3] A. Nicosia, T. Duchesne, L. P. Rivest, and D. Fortin, A general hidden state random walk model for animal movement, Comput. Stat. Data Anal. **105**, 76 (2017).

[4] J. D. Bailey, J. Wallis, and E. A. Codling, Navigational efficiency in a biased and correlated random walk model of individual animal movement, Ecology **99**, 217 (2018).

[5] H. Fritz, S. Said, and H. Weimerskirch, Scale-dependent hierarchical adjustments of movement patterns in a long-range foraging seabird, Proc. R. Soc. B **270**, 1143 (2003).

[6] G. H. Pyke, Understanding movements of organisms: It's time to abandon the Lévy foraging hypothesis, Methods Ecol. Evol. **6**, 1 (2015).

[7] S. Benhamou and J. Collet, Ultimate failure of the Lévy foraging hypothesis: Two-scale searching strategies outperform scale-free ones even when prey are scarce and cryptic, J. Theor. Biol. **387**, 221 (2015).

[8] S. Benhamou, How many animals really do the Lévy walk?, Ecology **88**, 1962 (2007).

[9] G. M. Viswanathan, S. V. Buldyrev, S. Havlin, M. G. E. Da Luz, E. P. Raposo, and H. E. Stanley, Optimizing the success of random searches, Nature **401**, 911 (1999).

[10] P. G. Blackwell, M. Niu, M. S. Lambert, and S. D. Lapoint, Exact Bayesian inference for animal movement in continuous time, Methods Ecol. Evol. **7**, 184 (2016).

[11] O. Ovaskainen, Habitat-specific movement parameters estimated using mark-recapture data and a diffusion model, Ecology **85**, 242 (2004).

[12] S. Benhamou, Detecting an orientation component in animal paths when the preferred direction is individual-dependent, Ecology **87**, 518 (2006).

[13] S. Benhamou, Spatial memory and searching efficiency, Anim. Behav. **47**, 1423 (1994).

[14] F. Lenz, T. C. Ings, L. Chittka, A. V. Chechkin, and R. Klages, Spatiotemporal Dynamics of Bumblebees Foraging under Predation Risk, Phys. Rev. Lett. **108**, 098103 (2012).

[15] T. Adam, C. A. Griffiths, V. Leos-Barajas, E. N. Meese, C. G. Lowe, P. G. Blackwell, D. Righton, and R. Langrock, Joint modelling of multi-scale animal movement data using hierarchical hidden Markov models, Methods Ecol. Evol. **10**, 1536 (2019).

[16] K. Whoriskey, M. Auger-Méthé, C. M. Albertsen, F. G. Whoriskey, T. R. Binder, C. C. Krueger, and J. Mills Flemming, A hidden Markov movement model for rapidly identifying behavioral states from animal tracks, Ecol. Evol. **7**, 2112 (2017).

[17] R. Metzler, J. H. Jeon, A. G. Cherstvy, and E. Barkai, Anomalous diffusion models and their properties: Non-stationarity, non-ergodicity, and ageing at the centenary of single particle tracking, Phys. Chem. Chem. Phys. **16**, 24128 (2014).

[18] G. Afek, J. Coslovsky, A. Courvoisier, O. Livneh, and N. Davidson, Observing Power-Law Dynamics of Position-Velocity Correlation in Anomalous Diffusion, Phys. Rev. Lett. **119**, 060602 (2017).

[19] S. Ahlberg, T. Ambjörnsson, L. Lizana, M. Gerlach, E. G. Altmann, K. Speckner, M. Weiss, P. M. Riechers, J. P. Crutchfield, S. Sadegh, *et al.*, $1/f$ noise for intermittent quantum dots exhibits non-stationarity and critical exponents, New J. Phys. **16**, 113054 (2014).

[20] P. A. Frantsuzov, S. Volkán-Kacsó, and B. Jankó, Universality of the fluorescence intermittency in nanoscale systems: Experiment and theory, Nano Lett. **13**, 402 (2013).

[21] M. Pelton, D. G. Grier, and P. Guyot-Sionnest, Characterizing quantum-dot blinking using noise power spectra, Appl. Phys. Lett. **85**, 819 (2004).

[22] D. Krapf, Nonergodicity in nanoscale electrodes, Phys. Chem. Chem. Phys. **15**, 459 (2012).

[23] C. K. Peng, J. Mietus, J. M. Hausdorff, S. Havlin, H. E. Stanley, and A. L. Goldberger, Long-Range Anticorrelations and Non-Gaussian Behavior of the Heartbeat, Phys. Rev. Lett. **70**, 1343 (1993).

[24] A. W. Rempel, E. D. Waddington, J. S. Wettlaufer, and M. G. Worster, Possible displacement of the climate signal in ancient ice by premelting and anomalous diffusion, Nature **411**, 568 (2001).

[25] B. Tóth, Y. Lempérière, C. Deremble, J. De Lataillade, J. Kockelkoren, and J. P. Bouchaud, Anomalous price impact and the critical nature of liquidity in financial markets, Phys. Rev. X **1**, 021006 (2011).

[26] C. Di Rienzo, V. Piazza, E. Gratton, F. Beltram, and F. Cardarelli, Probing short-range protein Brownian motion in the cytoplasm of living cells, Nat. Commun. **5**, 5891 (2014).

[27] K. Norregaard, R. Metzler, C. M. Ritter, K. Berg-Sørensen, and L. B. Oddershede, Manipulation and motion of organelles and single molecules in living cells, Chem. Rev. **117**, 4342 (2017).

[28] S. M. A. Tabei, S. Burov, H. Y. Kim, A. Kuznetsov, T. Huynh, J. Jureller, L. H. Philipson, A. R. Dinner, and N. F. Scherer, Intracellular transport of insulin granules is a subordinated random walk, Proc. Natl. Acad. Sci. U. S. A. **110**, 4911 (2013).

[29] J. H. Jeon, V. Tejedor, S. Burov, E. Barkai, C. Selhuber-Unkel, K. Berg-Sørensen, L. Oddershede, and R. Metzler, *In Vivo* Anomalous Diffusion and Weak Ergodicity Breaking of Lipid Granules, Phys. Rev. Lett. **106**, 048103 (2011).

[30] D. Krapf, N. Lukat, E. Marinari, R. Metzler, G. Oshanin, C. Selhuber-Unkel, A. Squarcini, L. Stadler, M. Weiss, and X. Xu, Spectral content of a single non-Brownian trajectory, Phys. Rev. X **9**, 011019 (2019).

[31] S. Sadegh, J. L. Higgins, P. C. Mannion, M. M. Tamkun, and D. Krapf, Plasma membrane is compartmentalized by a self-similar cortical actin meshwork, Phys. Rev. X **7**, 011031 (2017).

[32] R. Metzler, J. H. Jeon, and A. G. Cherstvy, Non-Brownian diffusion in lipid membranes: Experiments and simulations, Biochim. Biophys. Acta, Biomembr. **1858**, 2451 (2016).
[33] J. H. Jeon, M. Javanainen, H. Martinez-Seara, R. Metzler, and I. Vattulainen, Protein crowding in lipid bilayers gives rise to non-Gaussian anomalous lateral diffusion of phospholipids and proteins, Phys. Rev. X **6**, 021006 (2016).
[34] D. Krapf, Mechanisms underlying anomalous diffusion in the plasma membrane, Curr. Top. Membr. **75**, 167 (2015).
[35] A. Hernandez-Agreda, R. D. Gates, and T. D. Ainsworth, Defining the core microbiome in corals' microbial soup, Trends Microbiol. **25**, 125 (2017).
[36] D. R. Bellwood, T. P. Hughes, C. Folke, and M. Nyström, Confronting the coral reef crisis, Nature **429**, 827 (2004).
[37] S. Li, L. M. Roger, L. Kumar, N. A. Lewinski, J. Klein-Seetharaman, A. Gagnon, H. M. Putnam, and J. Yang, Digital image processing to detect subtle motion in stony coral, Sci. Rep. **11**, 7722 (2021).
[38] J. E. Samson, L. A. Miller, D. Ray, R. Holzman, U. Shavit, and S. Khatri, A novel mechanism of mixing by pulsing corals, J. Exp. Biol. **222**, jeb192518 (2019).
[39] M. Kremien, U. Shavit, T. Mass, and A. Genin, Benefit of pulsation in soft corals, Proc. Natl. Acad. Sci. U. S. A. **110**, 8978 (2013).
[40] P. P. Laissue, L. Roberson, Y. Gu, C. Qian, and D. J. Smith, Long-term imaging of the photosensitive, reef-building coral *Acropora muricata* using light-sheet illumination, Sci. Rep. **10**, 10369 (2020).
[41] T. Wijgerde, C. I. F. Silva, V. Scherders, J. Van Bleijswijk, and R. Osinga, Coral calcification under daily oxygen saturation and PH dynamics reveals the important role of oxygen, Biol. Open **3**, 489 (2014).
[42] T. Wijgerde, A. Van Melis, C. I. F. Silva, M. C. Leal, L. Vogels, C. Mutter, and R. Osinga, Red light represses the photophysiology of the Scleractinian Coral *Stylophora pistillata*, PLoS One **9**, e92781 (2014).
[43] M. Nishita, S. Y. Park, T. Nishio, K. Kamizaki, Z. Wang, K. Tamada, T. Takumi, R. Hashimoto, H. Otani, G. J. Pazour, *et al.*, Ror2 signaling regulates Golgi structure and transport through IFT20 for tumor invasiveness, Sci. Rep. **7**, 1 (2017).
[44] N. A. Kamenos and S. J. Hennige, Reconstructing four centuries of temperature-induced coral bleaching on the Great Barrier Reef, Front. Mar. Sci. **5**, 283 (2018).
[45] N. R. Mollica, W. Guo, A. L. Cohen, K. F. Huang, G. L. Foster, H. K. Donald, and A. R. Solow, Ocean acidification affects coral growth by reducing skeletal density, Proc. Natl. Acad. Sci. U. S. A. **115**, 1754 (2018).
[46] Y. Rosenberg, T. Doniger, and O. Levy, Sustainability of coral reefs are affected by ecological light pollution in the Gulf of Aqaba/Eilat, Commun. Biol. **2**, 289 (2019).
[47] O. H. Shapiro, E. Kramarsky-Winter, A. R. Gavish, R. Stocker, and A. Vardi, A coral-on-a-chip microfluidic platform enabling live-imaging microscopy of reef-building corals, Nat. Commun. **7**, 10860 (2016).
[48] L. M. Roger, H. G. Reich, E. Lawrence, S. Li, W. Vizgaudis, N. Brenner, L. Kumar, J. Klein-Seetharaman, J. Yang, H. M. Putnam, *et al.*, Applying model approaches in non-model systems: A review and case study on coral cell culture, PLoS One **16**, e0248953 (2021).
[49] T. L. Hedrick, Software techniques for two- and three-dimensional kinematic measurements of biological and biomimetic systems, Bioinspir. Biomim. **3**, 034001 (2008).
[50] R. Kubo, The fluctuation-dissipation theorem, Rep. Prog. Phys. **29**, 255 (1966).
[51] H. Lei, N. A. Baker, and X. Li, Data-driven parameterization of the generalized Langevin equation, Proc. Natl. Acad. Sci. U. S. A. **113**, 14183 (2016).
[52] F. Grogan, H. Lei, X. Li, and N. A. Baker, Data-driven molecular modeling with the generalized Langevin equation, J. Comput. Phys. **418**, 109633 (2020).
[53] M. Chen, X. Li, and C. Liu, Computation of the memory functions in the generalized Langevin models for collective dynamics of macromolecules, J. Chem. Phys. **141**, 064112 (2014).
[54] A. M. Edwards, Using likelihood to test for Lévy flight search patterns and for general power-law distributions in nature, J. Anim. Ecol. **77**, 1212 (2008).
[55] A. M. Edwards, R. A. Phillips, N. W. Watkins, M. P. Freeman, E. J. Murphy, V. Afanasyev, S. V. Buldyrev, M. G. E. Da Luz, E. P. Raposo, H. E. Stanley, *et al.*, Revisiting Lévy flight search patterns of wandering albatrosses, bumblebees and deer, Nature **449**, 1044 (2007).
[56] https://doi.org/10.17605/OSF.IO/ZC5R9.